Localization Dynamics at the Exceptional Point of Non-Hermitian Creutz Ladder

S. M. Zhang(张舒迈)†, T. Y. He(何天毅)†, and L. Jin(金亮)*

School of Physics, Nankai University, Tianjin 300071, China

(Received 17 November 2023; accepted manuscript online 5 January 2024)

We propose a quasi-one-dimensional non-Hermitian Creutz ladder with an entirely flat spectrum by introducing alternating gain and loss components while maintaining inversion symmetry. Destructive interference generates a flat spectrum at the exceptional point, where the Creutz ladder maintains coalesced and degenerate eigenvalues with compact localized states distributed in a single plaquette. All excitations are completely confined within the localization area, unaffected by gain and loss. Single-site excitations exhibit nonunitary dynamics with intensities increasing due to level coalescence, while multiple-site excitations may display oscillating or constant intensities at the exceptional point. These results provide insights into the fascinating dynamics of non-Hermitian localization, where level coalescence and degeneracy coexist at the exceptional point.

DOI: 10.1088/0256-307X/41/2/027201

Spatial reflection ($\mathcal{P}$) and time-reversal ($\mathcal{T}$) symmetries work cooperatively as the combined parity-time ($\mathcal{PT}$) symmetry.[1–5] If the $\mathcal{PT}$ operator and the non-Hermitian Hamiltonian commute, they share the same set of eigenvectors and the Hamiltonian is $\mathcal{PT}$-symmetric.[6,7] The $\mathcal{PT}$ symmetry undergoes a transition from the exact $\mathcal{PT}$-symmetric phase with a real energy spectrum to the broken $\mathcal{PT}$-symmetric phase with an imaginary energy spectrum at the exceptional point (EP),[8–13] where eigenstate coalescence occurs.[14–16] The EPs in non-Hermitian physics have found extensive applications in optical sensing,[17–23] robust energy transfer,[24] and unidirectional dynamics.[25–34] Photonic structures are favorable in the investigation of the non-Hermitian physics. Recent advances in non-Hermitian physics have highlighted deviations from the established principle of bulk-boundary correspondence,[35–38] with new phenomena such as the non-Hermitian skin effect fundamentally changing the understanding of edge states.[39–44] These studies indicate that in non-Hermitian systems,[42–60] topological invariants and edge states are affected by unique symmetries and conditions, leading to unconventional localization phenomena.[38]

Flat bands are dispersionless and can be found in various one-dimensional (1D) and two-dimensional (2D) lattices. The eigenstate in the flat band is a compact localized state (CLS) that only localizes in a few unit cells.[61–67] CLSs exhibit stable dynamics in the time-evolution process and are advantageous for confining light in the context of light flow engineering. Optical waveguides created using direct femtosecond laser writing techniques have been extensively utilized to experimentally demonstrate flat bands.[68–71] In non-Hermitian systems, the flat bands are explored both theoretically and experimentally.[72–79] In quasi-1D lattices, flat bands persist with the addition of $\mathcal{PT}$-symmetric gain and loss,[72] while the system is in the exact (broken) $\mathcal{PT}$-symmetric phase through manipulating the gain/loss rate.[80] In addition, tunable flat bands are proposed in the 1D and 2D non-Hermitian lattices under destructive interference.[77,78] A photonic zero-mode flat band is predicted in the coupled photonic waveguide lattice.[76] The energy spectrum of the Aharonov–Bohm (AB) cage is fully composed of the flat bands,[81] any local excitation, not necessary to be in the form of CLSs, will be completely confined. The AB cage of a rhombic chain is constructed with half-quantum magnetic flux introduced in each diamond plaquette.[82–86] The AB cage has been experimentally observed in the femtosecond laser writing waveguide arrays.[82,83] Nonlinear dynamics and caging behavior are investigated in the presence of nonlinearity.[85–87]

The Creutz ladder is a fascinating quasi-1D lattice.[88,89] This lattice exhibits an entirely flat-band spectrum,[90] but the flat bands vanish when gain and loss are introduced separately in the two ladder legs.[47] However, when gain and loss are alternately introduced along both the ladder legs and the ladder rungs, the inversion symmetry is restored, allowing flat bands to potentially emerge under specific conditions. The inversion symmetric non-Hermitian Creutz ladder differs significantly from its counterpart without inversion symmetry. In the absence of the inversion symmetry, the interplay between synthetic magnetic flux and gain and loss leads to amplified unidirectional localization,[91] the breakdown of bulk-boundary correspondence,[39] and other intriguing results that diverge from traditional understandings in the Hermitian physics.[3,4,37,38] With the inversion symmetry intact, the destructive interference at the EP generates a flat-band spectrum. The arrangement of gain and loss significantly affects the band structure and the localization dynamics.

In this Letter, we investigate the flat bands and demonstrate the localization dynamics in a $\mathcal{PT}$-symmetric non-

†S. M. Zhang and T. Y. He contributed equally to this work.

*Corresponding author. Email: jinliang@nankai.edu.cn

© 2024 Chinese Physical Society and IOP Publishing Ltd

Hermitian Creutz ladder, which has alternately introduced gain and loss to ensure the inversion symmetry of the Creutz ladder. The half-quantum magnetic flux enclosed in each plaquette induces destructive interference at the EP, where all energy levels are either coalesced or degenerate. We conduct an analytical investigation of the intriguing non-Hermitian caging dynamics brought about by this destructive interference, supplemented by numerical simulations. We present excitation intensities that are constant, oscillating within bounds, or escalating polynomially. These are closely tied to the eigenstate orthogonality/nonorthogonality, as well as the degenerate, coalescent, and generalized eigenstates at the EP. Notably, in contrast to expansion, the area of localization remains unaffected by non-Hermiticity.

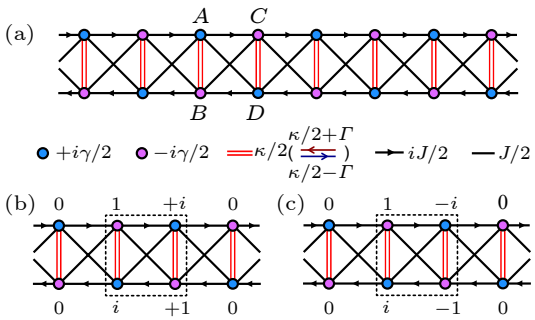

Fig. 1. (a) Schematic of the non-Hermitian Creutz ladder. Asymmetric couplings in the bracket are downward (upward) for $\kappa/2+\Gamma$ ($\kappa/2-\Gamma$). (b) CLS with flat-band energy J at the EP condition $\gamma=\kappa$. (c) CLS with flat-band energy $-J$ at the EP condition $\gamma=\kappa$. Both the CLSs are confined in a single plaquette enclosed by a black dotted box.

Inversion Symmetric Non-Hermitian Creutz Ladder. The Creutz ladder has been experimentally realized in circuits, cold-atom setups, and optical systems.[89,92–94] The quantum circuit closely relying on superconducting quantum interference device is utilized to obtain the geometry of the Creutz ladder.[93,94] Considering a cold-atom system, the Creutz ladder is proposed by two spatially overlapped optical zigzag lattices.[92] In addition, the s and p orbitals of ultracold atoms can simulate the two legs of the Creutz ladder, with cross couplings denoted by interorbital links introduced by lattice shaking.[89] In an optical lattice, two electromagnetic modes arising from a row of waveguides are dedicated to playing the role of two legs, and the cross links appear in a synthetic dimension. The Creutz ladder can also be obtained by employing the topological connection between the Creutz ladder and diamond chain, with energy offset in sites with four connections of the photonic diamond lattice.[82] The non-Hermitian Creutz ladder under consideration is depicted in Fig. 1(a). The gain and loss rates, alternately introduced to maintain the ladder's inversion symmetry, are denoted as γ. The synthetic magnetic flux is an essential ingredient to realize destructive interference and dispersionless energy spectrum.[95] The synthetic magnetic field has promoted the development of photonic crystals.[96] The Peierls phase is a significant element to realize a synthetic magnetic field, which can be generated through dynamics modulation[97] and path length imbalance.[98] In Fig. 1(a), the Peierls phase factor $e^{\pm i\pi/2}$ presents in the nonreciprocal coupling $\pm iJ/2$.[99] Nonreciprocal couplings have many experimental implementation in photonic systems.[98,100–102] When photons tunnel along the black arrows, they acquire an additional $e^{i\pi/2}$ phase factor; while tunneling against the black arrows, they acquire an additional phase factor $e^{-i\pi/2}$.[29] Therefore, in each unit cell of the non-Hermitian Creutz ladder, an effective π magnetic flux is enclosed in the square plaquette.

The red solid lines in Fig. 1(a) indicate the symmetric coupling $\kappa/2$ when $\Gamma=0$ between the ladder legs. When $\Gamma\neq 0$, the dark red arrow in the bracket is downward, indicating a tunneling strength of $\kappa/2+\Gamma$ from the upper ladder site to the lower ladder site; and the dark cyan arrow in the bracket is upward, indicating a tunneling strength of $\kappa/2-\Gamma$ from the lower ladder site to the upper ladder site; the nonzero Γ indicates asymmetric coupling between the ladder legs. The inversion symmetric non-Hermitian Creutz ladder also has $\mathcal{PT}$ symmetry.

The Bloch Hamiltonian of the non-Hermitian Creutz ladder is

$$H(k)=\begin{pmatrix} A & B(k) \\ B^{\dagger}(k) & C \end{pmatrix}, \tag{1}$$

where $A=\kappa\sigma_x/2-i\Gamma\sigma_y+i\gamma\sigma_z/2$, $B(k)=Je^{-ik/2}[\sigma_x\cos(k/2)+\sigma_z\sin(k/2)]$, and $C=\kappa\sigma_x/2-i\Gamma\sigma_y-i\gamma\sigma_z/2$. The energy bands are obtained in the form of

$$E(k)=\pm\sqrt{J^2-\Gamma^2+\frac{\kappa^2-\gamma^2}{4}\pm J\sqrt{\kappa^2-\gamma^2}\cos(k/2)}. \tag{2}$$

Energy levels coalesce at the EP when the condition $\gamma=\kappa$ is met. At the EP, the energy bands are completely flat with momentum independent band energies $\pm\sqrt{J^2-\Gamma^2}$. If the condition $J=\Gamma$ is also satisfied, the EP transforms into a high-order EP of order 4 where all energy levels are coalesced to zero energy. Figure 2 depicts the energy bands, with black circles denoting the flat-band energies. At the EP $\gamma=\kappa$, the lattice exhibits two-state coalescence as illustrated in Figs. 2(a)–2(d). In Figs. 2(e) and 2(f) for the gain and loss $\Gamma=J$, the lattice supports four-state coalescence in which the corresponding dimers are also at their own EP.[15]

At the EP $\gamma=\kappa$, the two flat bands with opposite energies correspond to two types of compact localized eigenstates of the non-Hermitian Creutz ladder. In Figs. 1(b) and 1(c), the two types of (unnormalized) compact localized eigenstates for $\Gamma=0$ are illustrated; the flat-band energies are $+J$ and $-J$, respectively. Two types of CLSs are obtained as follows, which satisfy the discrete time-independent Schrödinger equation

$$H\Psi_{\pm}=E_{\pm}\Psi_{\pm}, \tag{3}$$

where H is the Hamiltonian of the non-Hermitian Creutz ladder in Fig. 1(a); $\Psi_{\pm}$ is the wavefunction for the flat-band eigenenergy $E_{\pm}$. From the Schrödinger equation, the CLSs can be verified to be the eigenstates of H by checking the wavefunction amplitudes for all sites in the non-Hermitian

Creutz ladder. For instance, consider a CLS entirely confined within the plaquette in two unit cells, delineated by a dashed box in Figs. 1(b) and 1(c). Site A in the left unit cell couples to the two sites of the left $\mathcal{PT}$-symmetric dimer in the plaquette. The coupling from site C in the left unit cell with amplitude 1 to site A in the left unit cell is $-iJ/2$; the coupling from site D in the left unit cell with amplitude i to site A in the left unit cell is $J/2$. Thus, the amplitudes 1 and i on the left $\mathcal{PT}$-symmetric dimer in the plaquette induces destructive interference on site A in the left unit cell

$$(-iJ/2)\cdot(1)+(J/2)\cdot(i)=0, \tag{4}$$

which is the left side of the Schrödinger equation for the amplitude of site A in the left unit cell. Thus, the amplitude of site A in the left unit cell vanishes. Similarly, one can verify that the amplitudes of all sites outside the dashed plaquette vanish.

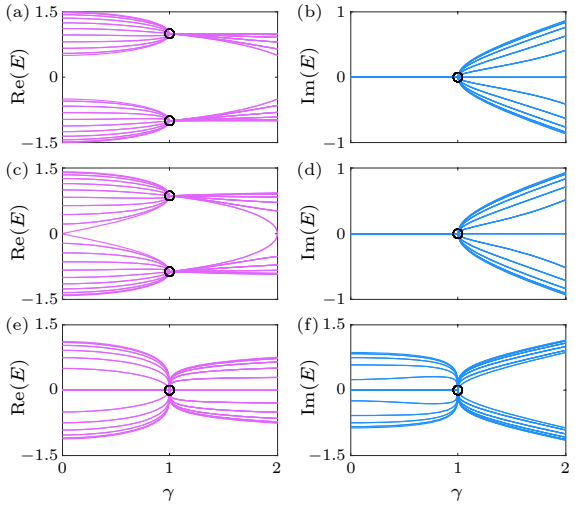

Fig. 2. Energy levels of Figs. 1(a) and 1(b) with different gain and loss rates under periodic boundary condition. [(a), (c), (e)] The real parts of spectra on the left panel are in magenta. [(b), (d), (f)] The imaginary parts on the right panel are in cyan. The black hollow circles indicate the fully flat energy bands at the EP when $\kappa=\gamma$, which induces the non-Hermitian AB cage. The parameters are $J=\kappa=1$ at [(a), (b)] $\Gamma=0$ with flat-band energies ±1, [(c), (d)] $\Gamma=1/2$ with flat-band energies $\pm\sqrt{3}/2$, and [(e), (f)] $\Gamma=1$ with flat-band energy 0. The lattice size is 40 with 10 unit cells in total.

After checking the validity of the discrete Schrödinger equations for the four sites inside the dashed plaquette, we can obtain the energy of the corresponding compact localized eigenstate and verify the CLSs as the eigenstates of the flat band.

The discrete Schrödinger equations for the sites in the dashed plaquette from the top-left and bottom-left to top-right and bottom-right are

$$\frac{J}{2}\cdot(\pm1)-\frac{iJ}{2}\cdot(\pm i)+\frac{\kappa}{2}\cdot i=\left(E+\frac{i\gamma}{2}\right)\cdot1, \tag{5}$$

$$\frac{J}{2}\cdot(\pm i)+\frac{iJ}{2}\cdot(\pm1)+\frac{\kappa}{2}\cdot1=\left(E-\frac{i\gamma}{2}\right)\cdot i, \tag{6}$$

$$\frac{J}{2}\cdot i+\frac{iJ}{2}\cdot1+\frac{\kappa}{2}\cdot(\pm1)=\left(E-\frac{i\gamma}{2}\right)\cdot(\pm i), \tag{7}$$

$$\frac{J}{2}\cdot1-\frac{iJ}{2}\cdot i+\frac{\kappa}{2}\cdot(\pm i)=\left(E+\frac{i\gamma}{2}\right)\cdot(\pm1). \tag{8}$$

The energy of the flat band is $E=J$ for the CLS shown in Fig. 1(b) and $E=-J$ for the CLS shown in Fig. 1(c). These CLSs are confined within a single square plaquette, with the wavefunctions being zero at all sites outside the plaquette. This localization results from complete destructive interference, facilitated by the combined effects of the Peierls phase, gain and loss, and the coupling strengths. Notably, all the other CLSs can be obtained in this manner; each plaquette supports two CLSs as shown in Figs. 1(b) and 1(c). The CLSs localized in different plaquettes are orthogonal; the only two supported eigenstates in each plaquette shows evidence of the deficiency of one-half energy levels.

The completely flat-band spectrum at the EP $\gamma=\kappa$ indicates that the complete confinement is supported by the non-Hermitian Creutz ladder, which is an AB cage. This is reflected from the compact localized eigenstates and the dynamics of excitations. The unique band structure and eigenstates give rise to intriguing localization dynamics within a non-Hermitian framework. Therefore, we refer to the non-Hermitian Creutz ladder as a non-Hermitian AB cage. At the EP, the energy levels are degenerate in addition to the coalescence. Half of the energy levels are deficient because of the two-state coalescence. The coalesced eigenstates within the same energy band are degenerate, while those associated with distinct eigenenergy values remain orthogonal, which is a feature of the non-Hermitian Creutz ladder. The orthogonality between eigenstates provides the possibility that Hermitian dynamics may appear in this system.[103] The CLSs are independent of the parameters γ and κ at the EP and remain unchanged across various $\gamma=\kappa$ conditions. Nevertheless, their dynamics are sensitive to and differ from the values of $\gamma=\kappa$. The non-Hermitian Creutz ladder, in which both gain and loss, as well as vertical couplings between the ladder legs, are removed ($\gamma=\kappa=\Gamma=0$), reduces to a Hermitian AB cage of a cross-stitched lattice.

Dynamics at the Exceptional Point. We exhibit the AB caging dynamics in the inversion-symmetric non-Hermitian Creutz ladder for different excitations at the EP, where a large number of level coalescences and degeneracies simultaneously occur. The time-evolution dynamics is analytically obtained, and the performed numerical simulation verifies the analytical prediction. The destructive interference at the EP generates the non-Hermitian AB caging; the intensity of excitation can be constant, oscillating, polynomially increasing, and polynomially increasing with oscillation. In the non-Hermitian Creutz ladder, the local excitation is completely confined because of the CLSs for the entirely flat spectrum. In contrast to expanding the localization area,[104] the non-Hermitian elements in the Creutz ladder does not affect the localization area, generate polynomially increasing intensity, and induce power oscillation. Each excitation is a superposition of single-site excitation. For single-site excitation, the excitation will be confined within two plaquettes as a consequence of

the CLSs.

In systems with fully flat bands, introducing uncorrelated on-site static disorder fails to disrupt the localization or induce the inverse Anderson transition.[105] However, correlated on-site static disorder can facilitate transport.[106] For the symmetric disorder ($\Delta_{n,A} = \Delta_{n,B}$, $\Delta_{n,C} = \Delta_{n,D}$), the non-defective degeneracies are lifted, yet the defective degeneracies are preserved, with the localization properties unaffected. For the anti-symmetric disorder ($\Delta_{n,A} = -\Delta_{n,B}$, $\Delta_{n,C} = -\Delta_{n,D}$), all the degeneracies are lifted, and the inverse Anderson transition is induced.[107]

The non-Hermitian AB cage is formed at the EP $\gamma = \kappa$, which is the $\mathcal{PT}$-symmetric phase transition point, and the non-Hermitian lattice becomes defective and unable to be diagonalized. Thus, the time-evolution dynamics cannot be obtained in the traditional manner from the expansion of the non-Hermitian Hamiltonian using the biorthogonal basis.[103] In the following, we show how to calculate the time evolution of the non-Hermitian AB cage.

The CLSs are confined within a single unit cell of the non-Hermitian Creutz ladder, and each single-site excitation is associated with only two adjacent unit cells. This implies that any single-site excitation remains restricted within two unit cells of the ladder. Consequently, the dynamical evolution of any single-site excitation can be determined using the eight-site non-Hermitian Hamiltonian H representing these two unit cells. Moreover, the non-Hermitian Creutz ladder constitutes a linear system in which the dynamics of any initial excitation are represented as a superposition of single-site excitation dynamics. Therefore, the time-evolution of any initial excitation can be inferred from the behavior of single-site excitations.

The discrete Schrödinger equation for the non-Hermitian ladder Hamiltonian H is

$$\frac{i\mathrm{d}\Psi(t)}{\mathrm{d}t} = H\Psi(t). \tag{9}$$

To calculate the AB caging dynamics at the EP, we first reduce the non-Hermitian Hamiltonian H into a Jordan block form h through a similar transformation

$$H = VhV^{-1}. \tag{10}$$

From $i\mathrm{d}\Psi(t)/\mathrm{d}t = H\Psi(t)$, we obtain the discrete Schrödinger equation for the Jordan block form Hamiltonian h in the form of

$$\frac{i\mathrm{d}\psi(t)}{\mathrm{d}t} = h\psi(t), \tag{11}$$

where $\Psi(t)$ and $\psi(t)$ are on behalf of the time-evolution states for H and h, respectively.

The initial state $\psi(0)$ for h is obtained from

$$\psi(0) = V^{-1}\Psi(0). \tag{12}$$

Then, the time-evolution state $\psi(t)$ is acquired from solving the differential Eq. (11) of the Jordan block form Hamiltonian h. Finally, we calculate the time-evolution dynamics in the original non-Hermitian Hamiltonian $\Psi(t)$ from the time-evolution dynamics in the Jordan-form Hamiltonian h through the similar transformation V,

$$\Psi(t) = V\psi(t). \tag{13}$$

We introduce the analytical calculation of the time-evolution dynamics of the non-Hermitian AB cage for the single-site initial excitation. For example, we consider the non-Hermitian Creutz ladder at the EP $\gamma = \kappa = 1$. In Section A of the Supplementary Material, we provide a detailed account of the process for reducing the eight-site non-Hermitian Hamiltonian H including two plaquettes of the Creutz ladder into the Jordan block form h via the similar transformation V. The schematic of H is also shown for clarity. The eigenstates coalesce at the EP and the Hamiltonian H is defective with two eigenstates missing. Substituting the time-evolution state $\psi(t) = [\psi_1(t), \ldots, \psi_8(t)]^{\mathrm{T}}$ into the discrete Schrödinger Eq. (11), the corresponding eight differential equations can be written as

$$\frac{i\mathrm{d}\psi_1(t)}{\mathrm{d}t} = -E\psi_1(t), \quad \frac{i\mathrm{d}\psi_2(t)}{\mathrm{d}t} = \psi_1(t) - E\psi_2(t), \tag{14}$$

$$\frac{i\mathrm{d}\psi_3(t)}{\mathrm{d}t} = E\psi_3(t), \quad \frac{i\mathrm{d}\psi_4(t)}{\mathrm{d}t} = \psi_3(t) + E\psi_4(t), \tag{15}$$

$$\frac{i\mathrm{d}\psi_5(t)}{\mathrm{d}t} = -E\psi_5(t), \quad \frac{i\mathrm{d}\psi_6(t)}{\mathrm{d}t} = E\psi_6(t), \tag{16}$$

$$\frac{i\mathrm{d}\psi_7(t)}{\mathrm{d}t} = -E\psi_7(t), \quad \frac{i\mathrm{d}\psi_8(t)}{\mathrm{d}t} = E\psi_8(t). \tag{17}$$

Solving these differential equations, we obtain the expression

$$\begin{aligned}\psi(t) = [&c_1 e^{iEt}, (-it)c_1 e^{iEt} + c_2 e^{iEt}, c_3 e^{-iEt}, (-it)c_3 e^{-iEt} \\ &+ c_4 e^{-iEt}, c_5 e^{iEt}, c_6 e^{-iEt}, c_7 e^{iEt}, c_8 e^{-iEt}]^{\mathrm{T}},\end{aligned} \tag{18}$$

for the initial state $\psi(0) = [c_1, c_2, c_3, c_4, c_5, c_6, c_7, c_8]^{\mathrm{T}}$. The coefficients c_1 to c_8 in the expression are determined from the initial state $\Psi(0)$ for H from Eq. (12).

We consider the dynamics in the non-Hermitian Creutz ladder at the additional parameters $J = 1$ and $\Gamma = 0$. The vertical couplings between ladder legs are symmetric. For a single-site initial excitation at site 5, the initial state for H is $\Psi(0) = [0, 0, 0, 0, 1, 0, 0, 0]^{\mathrm{T}}$, the corresponding initial state for h is expressed as $\psi(0) = (1/8)[-i, -i, -i, i, 4 + 2i, 4 - 2i, -4i, 4i]^{\mathrm{T}}$. The time-evolution state $\psi(t)$ is Eq. (18) with $E = 1$; then, the time-evolution state $\Psi(t) = V\psi(t)$ is acquired. The total intensity $I(t) = \langle\Psi(t)|\Psi(t)\rangle$ of the time-evolution state for H is analytically obtained as follows:

$$I(t) = \frac{1}{4}\Big[t^2 - 2\,t - \frac{1}{2}\cos(2\,t) - \sin(2\,t) + \frac{9}{2}\Big]. \tag{19}$$

The excitation intensity quadratically increases with time. This nonunitary dynamics is a typical feature of non-Hermitian systems as depicted in Fig. 3(a).[108,109] The excitation intensity of the quadratical growth is presented when involving the generalized eigenstate at the EP;[110,111] furthermore, though at the high-order EP, the increasing intensity has a more rapid polynomial growth that linearly scales with the order of EP.[112,113] If the initial state is the superposition of eigenstates with different energies, the intensity of the time-evolution state exhibits oscillation.[103]

For the non-Hermitian Creutz ladder at the additional parameters $J = 1$ and $\Gamma = 1/2$, the flat-band energies are $\pm\sqrt{3}/2$. We still consider the single-site initial

excitation $\Psi(0) = [0, 0, 0, 0, 1, 0, 0, 0]^{\mathrm{T}}$ in H, the initial state $\psi(0)$ for h is obtained from Eq. (12) as $\psi(0) = (\sqrt{3}/3)[-i\sqrt{3}/6, -i/3, -i\sqrt{3}/6, i/3, e^{i\pi/6}, e^{-i\pi/6}, -1, 1]^{\mathrm{T}}$. The time-evolution state $\Psi(t) = V\psi(t)$ is obtained from $\psi(t)$, and the corresponding intensity $I(t) = \langle\Psi(t)|\Psi(t)\rangle$ is

$$I(t) = \frac{1}{9}\Big[t^2\cos(\sqrt{3}t) - \sqrt{3}t^2\sin(\sqrt{3}t) + 4t^2 - 2t\cos(\sqrt{3}t) + \frac{2\sqrt{3}}{3}t\sin(\sqrt{3}t) - 4t - \sqrt{3}\sin(\sqrt{3}t) - \frac{13}{3}\cos(\sqrt{3}t) + \frac{40}{3}\Big]. \tag{20}$$

The excitation intensity quadratically increases as time does with periodic oscillation. This is depicted as the black curve in Fig. 3(b).

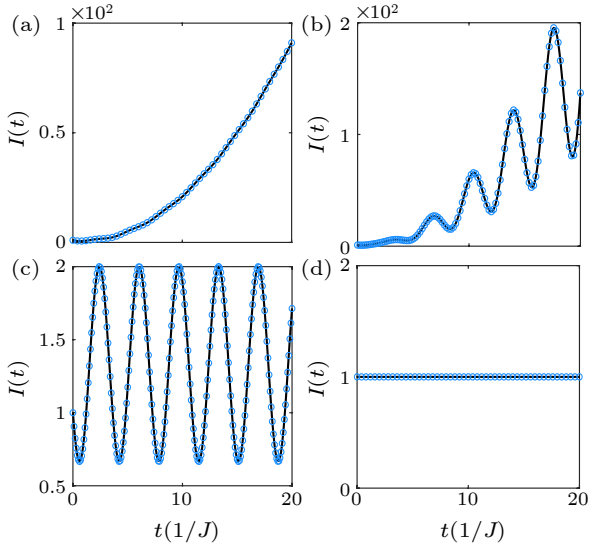

Fig. 3. Intensity of the time-evolution dynamics at different initial states and system parameters. The initial state is $\Psi(0) = [0, 0, 0, 0, 1, 0, 0, 0]^{\mathrm{T}}$ [(a), (b)] and $\Psi(0) = [0, 0, 0, 0, -i\sqrt{2}/2, \sqrt{2}/2, 0, 0]^{\mathrm{T}}$ [(c), (d)]. Analytical results are indicated by black solid curves; numerical results are indicated by blue stars. For each moment in (a), (b), (c), and (d), the analytical intensity is strictly depicted in Eqs. (19), (20), (21), and (22), respectively. The parameters are [(a), (d)] $\Gamma = 0$ and [(b), (c)] $\Gamma = 1/2$ with $J = \kappa = \gamma = 1$.

The time-evolution dynamics of single-site excitation in either of the four sites in a single plaquette can be analytically obtained. Consequently, any excitation can be obtained from the state superposition. For the non-Hermitian Creutz ladder with additional parameters $J = 1$ and $\Gamma = 1/2$, the initial state for H is chosen as $\Psi(0) = [0, 0, 0, 0, -i\sqrt{2}/2, \sqrt{2}/2, 0, 0]^{\mathrm{T}}$, being a superposition of states $[0, 0, 0, 0, 1, 0, 0, 0]^{\mathrm{T}}$ and $[0, 0, 0, 0, 0, 1, 0, 0]^{\mathrm{T}}$ with the superposition coefficients $-i\sqrt{2}/2$ and $\sqrt{2}/2$, respectively. The corresponding initial state for h obtained from Eq. (12) is $\psi(0) = (\sqrt{6}/6)[0, 0, 0, 0, e^{-i\pi/3}, -e^{i\pi/3}, e^{i\pi/6}, e^{-i\pi/6}]^{\mathrm{T}}$. Consequently, we obtain the oscillating intensity

$$I(t) = \frac{1}{3}[4 - \sqrt{3}\sin(\sqrt{3}t) - \cos(\sqrt{3}t)]. \tag{21}$$

The intensity is depicted in Fig. 3(c), being bounded and periodically oscillating.

For the above-mentioned superposition initial state $\Psi(0) = [0, 0, 0, 0, -i\sqrt{2}/2, \sqrt{2}/2, 0, 0]^{\mathrm{T}}$, we obtain the constant intensity in the non-Hermitian Creutz ladder at the additional parameters $J = 1$ and $\Gamma = 0$. The initial state for h is $\psi(0) = (\sqrt{2}/4)[0, 0, 0, 0, -i, -i, -1, 1]^{\mathrm{T}}$ and the corresponding intensity is

$$I(t) = 1. \tag{22}$$

The intensity is depicted in Fig. 3(d). The numerical excitation intensity is completely in accordance with analytical results for all four cases. The reason for constant intensity is that the excitation only involves orthogonal eigenstates.

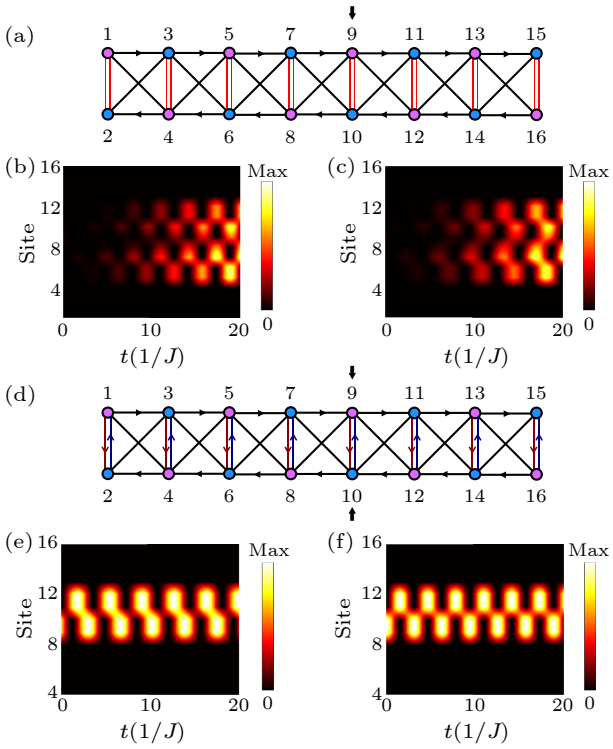

Fig. 4. [(a), (d)] Schematics of a 16-site non-Hermitian Creutz ladder. [(b), (c), (e), (f)] Time-evolution dynamics of the intensities on each site of the Creutz ladder. The corresponding total intensities are shown in Figs. 3(a), 3(b), 3(c), and 3(d), respectively. Black arrows above/below the two 16-site lattices indicate the excited sites at the initial moment $t = 0$. The parameters are chosen to be identical with those in Fig. 3.

Figure 4 depicts the time-evolution dynamics corresponding to the analytical results in Eqs. (19)–(22). To demonstrate the localization dynamics, we exhibit the time-evolution dynamics in a 16-site non-Hermitian Creutz ladder. The intensity for each site is fully exhibited and the intensity distribution is observed in the time evolution. The polynomial growth of total intensity is a unique feature of EP dynamics, which is unattainable in the systems not at the EPs. In the first two cases of Figs. 4(a) and 4(b), photon tunneling is permitted between sites 5 to 12 across two plaquettes. The intensity growth indicates that the coalescence in the flat band is a two-state coalescence and the EP is of order 2. Conversely, in the remaining cases of Figs. 4(c) and 4(d), photon tunneling is restricted to sites 9 to 12 within a single plaquette. The vertical

coupling asymmetry Γ induces oscillatory behavior in the excitation intensity with a period of $2\pi\sqrt{3}/3$ for involving the eigenstates from both the upper and lower bands. It is interesting that while the total intensity remains constant in the last scenario, the intensity at each individual site still exhibits oscillatory behavior identical to the unitary dynamics in Hermitian systems.

In Section B of the Supplementary Material, we analytically examine the excitation dynamics at the high-order EP with four-state coalesced at $\Gamma = J$. Here, the excitation intensity expands at a more rapid pace compared to that within the Creutz ladder at a two-state coalescence, exhibiting polynomial growth with respect to time at the order of six.

In summary, we have systematically investigated the intriguing localization dynamics in the $\mathcal{PT}$-symmetric non-Hermitian Creutz ladder with the inversion symmetry. The proper match between the synthetic magnetic flux and the balanced gain and loss at the EP results in fully destructive interference to generate a completely flat spectrum and the AB caging. Eigenstates are compactly localized within each single plaquette of the non-Hermitian Creutz ladder. Local excitations are completely confined, with the localization area being unaffected by non-Hermiticity. The eigenstates are coalesced and degenerate simultaneously. The lattice displays both unitary and nonunitary dynamics within the non-Hermitian AB cage at the EP, where excitation intensities exhibit constant, oscillating, polynomially increasing, and polynomially increasing with oscillation dynamics as a consequence of the eigenstate orthogonality/nonorthogonality, and the relevance with the degenerate eigenstates, coalesced eigenstates, and generalized eigenstates of the Creutz ladder. Our findings significantly contribute to the understanding of non-Hermitian localization dynamics at the EPs, particularly in contexts with extensive level coalescences and degeneracies.

Acknowledgement. This work was supported by the National Natural Science Foundation of China (Grant Nos. 12222504 and 11975128).

References

[1] Feng L, El-Ganainy R, and Ge L 2017 *Nat. Photon.* **11** 752
[2] Christodoulides D and Yang J 2018 *Parity-Time Symmetry and Its Applications* (Berlin: Springer)
[3] El-Ganainy R, Makris K G, Khajavikhan M, Musslimani Z H, Rotter S, and Christodoulides D N 2018 *Nat. Phys.* **14** 11
[4] Miri M A and Alù A 2019 *Science* **363** eaar7709
[5] Özdemir Ş K, Rotter S, Nori F, and Yang L 2019 *Nat. Mater.* **18** 783
[6] Jin L and Song Z 2009 *Phys. Rev. A* **80** 052107
[7] Jin L and Song Z 2010 *Phys. Rev. A* **81** 032109
[8] Luo X B, Huang J H, Zhong H H, Qin X Z, Xie Q T, Kivshar Y S, and Lee C 2013 *Phys. Rev. Lett.* **110** 243902
[9] Jin L and Song Z 2016 *Phys. Rev. A* **93** 062110
[10] Zhang K L, Jin L, and Song Z 2019 *Phys. Rev. B* **100** 144301
[11] Duan L W, Wang Y Z, and Chen Q H 2020 *Chin. Phys. Lett.* **37** 081101
[12] Fu T, Wang Y F, Wang X Y, Zhou X Y, and Zheng W H 2020 *Chin. Phys. Lett.* **37** 044207
[13] Xu H S and Jin L 2023 *Phys. Rev. Res.* **5** L042005
[14] Jin L 2018 *Phys. Rev. A* **97** 012121
[15] Zhang S M, Zhang X Z, Jin L, and Song Z 2020 *Phys. Rev. A* **101** 033820
[16] Jin L, Wu H C, Wei B B, and Song Z 2020 *Phys. Rev. B* **101** 045130
[17] Wiersig J 2014 *Phys. Rev. Lett.* **112** 203901
[18] Liu Z P, Zhang J, Özdemir Ş K, Peng B, Jing H, Lü X Y, Li C W, Yang L, Nori F, and Liu Y X 2016 *Phys. Rev. Lett.* **117** 110802
[19] Hodaei H, Hassan A U, Wittek S, Garcia-Gracia H, El-Ganainy R, Christodoulides D N, and Khajavikhan M 2017 *Nature* **548** 187
[20] Chen W J, Özdemir Ş K, Zhao G M, Wiersig J, and Yang L 2017 *Nature* **548** 192
[21] Chen C, Jin L, and Liu R B 2019 *New J. Phys.* **21** 083002
[22] Lai Y H, Lu Y K, Suh M G, Yuan Z, and Vahala K 2019 *Nature* **576** 65
[23] Hokmabadi M P, Schumer A, Christodoulides D N, and Khajavikhan M 2019 *Nature* **576** 70
[24] Xu H, Mason D, Jiang L, and Harris J G E 2016 *Nature* **537** 80
[25] Jin L and Song Z 2012 *Phys. Rev. A* **85** 012111
[26] Ramezani H, Li H K, Wang Y, and Zhang X 2014 *Phys. Rev. Lett.* **113** 263905
[27] Jin L, Zhang X Z, Zhang G, and Song Z 2016 *Sci. Rep.* **6** 20976
[28] Gear J, Sun Y, Xiao S, Zhang L, Fitzgerald R, Rotter S, Chen H, and Li J 2017 *New J. Phys.* **19** 123041
[29] Jin L and Song Z 2018 *Phys. Rev. Lett.* **121** 073901
[30] Luo J, Li J, and Lai Y 2018 *Phys. Rev. X* **8** 031035
[31] Jin L and Song Z 2021 *Chin. Phys. Lett.* **38** 024202
[32] Jin L 2022 *Chin. Phys. Lett.* **39** 037302
[33] Zhang K, Fang C, and Yang Z S 2023 *Phys. Rev. Lett.* **131** 036402
[34] Liu C, Lan J, Gu Z M, and Zhu J 2023 *Chin. Phys. Lett.* **40** 124301
[35] Ashida Y, Gong Z, and Ueda M 2020 *Adv. Phys.* **69** 249
[36] Bergholtz E J, Budich J C, and Kunst F K 2021 *Rev. Mod. Phys.* **93** 015005
[37] Ding K, Fang C, and Ma G 2022 *Nat. Rev. Phys.* **4** 745
[38] Lin R J, Tai T, Li L H, and Lee C H 2023 *Front. Phys.* **18** 53605
[39] Yao S Y and Wang Z 2018 *Phys. Rev. Lett.* **121** 086803
[40] Yao S Y, Song F, and Wang Z 2018 *Phys. Rev. Lett.* **121** 136802
[41] Song F, Yao S Y, and Wang Z 2019 *Phys. Rev. Lett.* **123** 246801
[42] Zhang K, Yang Z S, and Fang C 2020 *Phys. Rev. Lett.* **125** 126402
[43] Yang Z S, Zhang K, Fang C, and Hu J P 2020 *Phys. Rev. Lett.* **125** 226402
[44] Zhang K, Yang Z, and Fang C 2022 *Nat. Commun.* **13** 2496
[45] Jin L 2017 *Phys. Rev. A* **96** 032103
[46] Jin L, Wang P, and Song Z 2017 *Sci. Rep.* **7** 5903
[47] Jin L and Song Z 2019 *Phys. Rev. B* **99** 081103(R)
[48] Wu H C, Jin L, and Song Z 2019 *Phys. Rev. B* **100** 155117
[49] Lin S, Jin L, and Song Z 2019 *Phys. Rev. B* **99** 165148
[50] Zhang K L, Wu H C, Jin L, and Song Z 2019 *Phys. Rev. B* **100** 045141
[51] Xiao L, Deng T S, Wang K K, Zhu G Y, Wang Z, Yi W, and Xue P 2020 *Nat. Phys.* **16** 761
[52] Wang X R, Guo C X, Du Q, and Kou S P 2020 *Chin. Phys. Lett.* **37** 117303
[53] Wu H C, Yang X M, Jin L, and Song Z 2020 *Phys. Rev. B* **102** 161101(R)
[54] Wu H C, Jin L, and Song Z 2021 *Phys. Rev. B* **103** 235110
[55] Xie L C, Wu H C, Zhang X Z, Jin L, and Song Z 2021 *Phys. Rev. B* **104** 125406
[56] Li T Y, Zhang Y S, and Yi W 2021 *Chin. Phys. Lett.* **38** 030301
[57] Cao P C, Peng Y G, Li Y, and Zhu X F 2022 *Chin. Phys. Lett.* **39** 057801
[58] Wang J H, Tao Y L, and Xu Y 2022 *Chin. Phys. Lett.* **39** 010301

[59] Wang L W, Lin Z K, and Jiang J H 2023 *Phys. Rev. B* **108** 195126
[60] Liu Z F and Huang J P 2023 *Chin. Phys. Lett.* **40** 110305
[61] Masumoto N, Kim N Y, Byrnes T, Kusudo K, Löffler A, Höfling S, Forchel A, and Yamamoto Y 2012 *New J. Phys.* **14** 065002
[62] Flach S, Leykam D, Bodyfelt J D, Matthies P, and Desyatnikov A S 2014 *Europhys. Lett.* **105** 30001
[63] Bodyfelt J D, Leykam D, Danieli C, Yu X, and Flach S 2014 *Phys. Rev. Lett.* **113** 236403
[64] Jacqmin T, Carusotto I, Sagnes I, Abbarchi M, Solnyshkov D D, Malpuech G, Galopin E, Lemaître A, Bloch J, and Amo A 2014 *Phys. Rev. Lett.* **112** 116402
[65] Morales-Inostroza L and Vicencio R A 2016 *Phys. Rev. A* **94** 043831
[66] Leykam D, Andreanov A, and Flach S 2018 *Adv. Phys. X* **3** 1473052
[67] Zhang S M and Jin L 2020 *Phys. Rev. B* **102** 054301
[68] Guzmán-Silva D, Mejía-Cortés C, Bandres M A, Rechtsman M C, Weimann S, Nolte S, Segev M, Szameit A, and Vicencio R A 2014 *New J. Phys.* **16** 063061
[69] Mukherjee S and Thomson R R 2015 *Opt. Lett.* **40** 5443
[70] Vicencio R A, Cantillano C, Morales-Inostroza L, Real B, Mejía-Cortés C, Weimann S, Szameit A, and Molina M I 2015 *Phys. Rev. Lett.* **114** 245503
[71] Mukherjee S, Spracklen A, Choudhury D, Goldman N, Öhberg P, Andersson E, and Thomson R R 2015 *Phys. Rev. Lett.* **114** 245504
[72] Molina M I 2015 *Phys. Rev. A* **92** 063813
[73] Ge L 2015 *Phys. Rev. A* **92** 052103
[74] Ramezani H 2017 *Phys. Rev. A* **96** 011802(R)
[75] Biesenthal T, Kremer M, Heinrich M, and Szameit A 2019 *Phys. Rev. Lett.* **123** 183601
[76] Qi B, Zhang L, and Ge L 2018 *Phys. Rev. Lett.* **120** 093901
[77] Jin L 2019 *Phys. Rev. A* **99** 033810
[78] Zhang S M and Jin L 2019 *Phys. Rev. A* **100** 043808
[79] Zhang S M, Xu H S, and Jin L 2023 *Phys. Rev. A* **108** 023518
[80] Zhang X Z, Jin L, and Song Z 2012 *Phys. Rev. A* **85** 012106
[81] Vidal J, Mosseri R, and Douçot B 1998 *Phys. Rev. Lett.* **81** 5888
[82] Mukherjee S, Di Liberto M, Öhberg P, Thomson R R, and Goldman N 2018 *Phys. Rev. Lett.* **121** 075502
[83] Kremer M, Petrides I, Meyer E, Heinrich M, Zilberberg O, and Szameit A 2020 *Nat. Commun.* **11** 907
[84] Longhi S 2014 *Opt. Lett.* **39** 5892
[85] Gligorić G, Beličev P P, Leykam D, and Maluckov A 2019 *Phys. Rev. A* **99** 013826
[86] Di Liberto M, Mukherjee S, and Goldman N 2019 *Phys. Rev. A* **100** 043829
[87] Danieli C, Andreanov A, Mithun T, and Flach S 2021 *Phys. Rev. B* **104** 085131
[88] Cai H, Liu J, Wu J, He Y, Zhu S Y, Zhang J X, and Wang D W 2019 *Phys. Rev. Lett.* **122** 023601
[89] Kang J H, Han J H, and Shin Y 2020 *New J. Phys.* **22** 013023
[90] Kuno Y 2020 *Phys. Rev. B* **101** 184112
[91] Wang P, Jin L, and Song Z 2019 *Phys. Rev. A* **99** 062112
[92] Sun N and Lim L K 2017 *Phys. Rev. B* **96** 035139
[93] Alaeian H, Chang C W S, Moghaddam M V, Wilson C M, Solano E, and Rico E 2019 *Phys. Rev. A* **99** 053834
[94] Hung J S C, Busnaina J H, Chang C W S, Vadiraj A M, Nsanzineza I, Solano E, Alaeian H, Rico E, and Wilson C M 2021 *Phys. Rev. Lett.* **127** 100503
[95] Xu H S and Jin L 2022 *Phys. Rev. Res.* **4** L032015
[96] Ozawa T, Price H M, Amo A, Goldman N, Hafezi M, Lu L, Rechtsman M C, Schuster D, Simon J, Zilberberg O, and Carusotto I 2019 *Rev. Mod. Phys.* **91** 015006
[97] Goldman N and Dalibard J 2014 *Phys. Rev. X* **4** 031027
[98] Hafezi M 2014 *Int. J. Mod. Phys. B* **28** 1441002
[99] Xie L C, Jin L, and Song Z 2023 *Sci. Bull.* **68** 255
[100] Sounas D L and Alù A 2017 *Nat. Photon.* **11** 774
[101] Miri M A, Ruesink F, Verhagen E, and Alù A 2017 *Phys. Rev. Appl.* **7** 064014
[102] Fan L, Wang J, Varghese L T, Shen H, Niu B, Xuan Y, Weiner A M, and Qi M 2012 *Science* **335** 447
[103] Jin L and Song Z 2011 *Phys. Rev. A* **84** 042116
[104] Zhang S M and Jin L 2020 *Phys. Rev. Res.* **2** 033127
[105] Gligorić G, Leykam D, and Maluckov A 2020 *Phys. Rev. A* **101** 023839
[106] Longhi S 2021 *Opt. Lett.* **46** 2872
[107] Li H, Dong Z L, Longhi S, Liang Q, Xie D Z, and Yan B 2022 *Phys. Rev. Lett.* **129** 220403
[108] Zhan X, Xiao L, Bian Z, Wang K, Qiu X, Sanders B C, Yi W, and Xue P 2017 *Phys. Rev. Lett.* **119** 130501
[109] Wang K K, Qiu X Z, Xiao L, Zhan Z, Bian Z H, Sanders B C, Yi W, and Xue P 2019 *Nat. Commun.* **10** 2293
[110] Wang P, Jin L, Zhang G, and Song Z 2016 *Phys. Rev. A* **94** 053834
[111] Li C, Jin L, and Song Z 2017 *Phys. Rev. A* **95** 022125
[112] Zhong Q, Christodoulides D N, Khajavikhan M, Makris K G, and El-Ganainy R 2018 *Phys. Rev. A* **97** 020105(R)
[113] Xu H S, Xie L C, and Jin L 2023 *Phys. Rev. A* **107** 062209